

Work-function and structures of (100), (111) and (101) Au surfaces with/without oxygen

Yukio Watanabe^{1,2}, S. Miyauchi¹, S. Kaku¹, T. Yamada¹, and A. Horiguchi¹

¹Kyushu University, Fukuoka, Japan, ²University of Hyogo, Himeji, Japan

(100), (101), and (111) Au surfaces with chemisorbed oxygen of varying coverages are studied using density and hybrid functional theories and experiments. This clarifies the work function (ϕ), surface structures, stability, and density of states. ϕ of the (100), (101), and (111) Au surfaces calculated using the hybrid functional is 5.06–5.23 eV, respectively, and consistent with the reported experimental ϕ of polycrystalline Au films (5.1 ± 0.1 eV). The hybrid functional calculations on ϕ at (100) and (101) AuO surfaces agree with the experimental ϕ . In the reported and present experiments, the difference in ϕ between the Au and AuO surfaces ($\Delta\phi$) is 0.8–0.9 eV. However, the reported theoretical $\Delta\phi$ at (111) surface (3 eV) completely contradicts this value, which has been unresolved. We find that when O atoms are at (111) surface and subsurface, the theoretical $\Delta\phi$ at (111) agrees with experimental $\Delta\phi$ (0.8–0.9 eV). This state is considered to correspond to the experiments, because the oxygen-chemisorption is more stable in this state than when O atoms are at (111) surface only. This property is unique to the (111) surface. The prediction of chemisorbed-oxygen-induced disorders that are experimentally observed provides more evidence for the veracity of these calculations.

1. Introduction

Gold (Au), typically known for its chemical inertness, has shown potential for high catalytic activity when its surfaces are oxidized. This characteristic makes oxidized Au surfaces suitable for applications such as water splitting, offering a promising solution for the world's energy needs [1-3]. Furthermore, the crucial role of oxygen in chemical reactions at the Au surface has been well-documented, including its involvement in CO oxidation, alcohol oxidation, and propylene epoxidation [3]. Various methods, such as electrochemical processes, oxygen plasma, and ozone, have been successfully used to achieve the oxidation of Au surfaces [4-16].

To understand these properties, the work function (ϕ) [17], which determines the electron transfer between different materials, is fundamental. However, the density functional theories (DFT) studies of oxygen-chemisorbed Au surfaces have focused mainly on structural properties [18-22]. In particular, Sun et al. [18] and Daigle and BelBruno [22] clarified the dependence of the oxygen binding energy on the occupation site and surface orientation.

Contrastingly, reports on ϕ are scarce, except for the elaborated photoemission experiments by Saliba et al. [15] and Gottfried et al. [23] and the pioneering DFT study on ϕ at (111) surfaces by Shi and Stampfl [24]. Moreover, theoretical ϕ [24] completely disagrees with experimental ϕ [15, 23]. Hence, this paper reports experimental and *ab initio* studies on ϕ and the properties of the oxygen-chemisorbed (100), (111), and (101) Au surfaces using an accurate *ab initio* method.

For the measurements of ϕ of *in situ*-treated Au surfaces, we used Kelvin probe force microscopy (KPFM) in an ultra-high-vacuum (UHV) atomic force microscopy system [25]. This method is more sensitive to the top surface than X-ray photoemission spectroscopy (XPS).

Tran et al. [26] and De Waele et al. [27] show that the density functional theory (DFT) of ϕ of simple metals matches experimental values within 0.2–0.5 eV. However, for AuO_n (where $0 < n \leq 1$ and AuO is AuO_1), the error is significant because the difference in ϕ between Au and AuO_n ranges from 0.3 to 1 eV. Generally, *ab initio* calculations using hybrid functionals provide accurate electronic properties of oxides. Hence, we used DFT and hybrid functionals optimized for solids to calculate the oxygen-chemisorbed Au surfaces. These results help to understand the experimental and theoretical ϕ

values, as well as the stability and structures of oxygen-chemisorbed Au surfaces.

2. Methods

2.1. Experimental

Au films (100 nm thick) were sputter-deposited on BaTiO₃ single crystals at RT using 99.99% purity Ar gas and 99.9% purity Au target in a turbo-molecular-pumped vacuum chamber at a background pressure of $<10^{-3}$ Pa. The lattice constant of the fcc surface of Au (4.070 Å [28]) is close to those of BaTiO₃ (4.04 Å and 3.99 Å [29]), but the crystallographic orientation of the deposited Au films was not observed by X-ray diffraction. These films were taken out to air and then transferred to the treatment chamber of a UHV-SPM system (JEOL UHV-SPM 4610) and cleaned by burning out adsorbates with oxygen atoms (O) of 0.1 Pa at room temperature (RT) for 3 h. The elimination of adsorbates and the suppression of defect formation by this cleaning method were confirmed by X-ray photoemission [10,30], and the absence of interface material was indicated by the clear superconducting gap of YBa₂Cu₃O₇ [30]. Further, the ideal Schottky properties of the SrTiO₃:Nb surface obtained after this cleaning also proved the absence of defects and adsorbates [31].

These O atoms were produced by electron cyclotron resonance (ECR) from cryogenically re-purified O₂ of initially 99.9999% purity (highest commercial grade) at a flow rate of 2 SCCM (cc/min). From the emission spectra, it was determined that the emissions were of atomic O, except for negligible intensities of excited O₂ and O₃. If we assume the 100% conversion of O₂ to O, the cumulative area density of O atoms that arrived at the Au surface in 3 hours was 6.5×10^{20} cm⁻², i.e. 5.4×10^5 /unit-surface of Au (2.87² Å²) which an Au atom occupies. Hence, the O-atom coverage at the topmost Au surface was considered to be almost 100% because of the previous experimental studies [15,23]. The sufficient thermalization of the O gas was confirmed by the clear atomic steps of the substrate BaTiO₃ (Fig. 1).

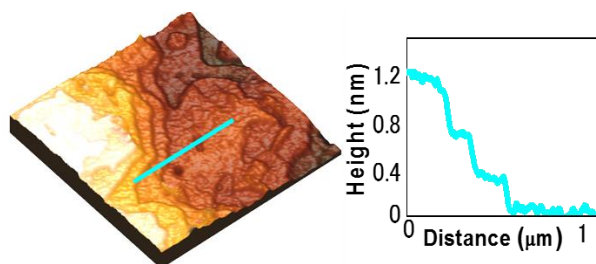


Fig. 1. Topography of a substrate (BaTiO₃) surface after atomic O exposure treatment.

ϕ was measured in the main chamber of a UHV-SPM 4610 using KPFM operated in a true-noncontact mode based on Van der Waals force. The probe of the KPFM was a cantilever made of very heavy-doped n-type Si (resistivity of 10–25 m Ω cm according to the manufacturer MikroMasch[®]). Native oxides and contaminants on the cantilever surface were removed by holding at 150 °C in the UHV treatment chamber for 6 h. The base pressure in the treatment chamber and the pressure in the main chamber were 2×10^{-7} Pa and $<2 \times 10^{-8}$ Pa, respectively. As a test of the cleanness of the main chamber, clear images of individual atoms on a Si [111] surface measured by noncontact SPM showed no change for at least a month.

2.2. *Ab initio* calculations

Ab initio calculations were performed using PAW potentials [32] implemented in VASP [33–35] with a plane wave energy cutoff of 650 eV. According to Perdew et al. [36], Perdew-Burke-Ernzerhof (PBE) functional optimized for solids (PBEsol) improves the accuracy of the equilibrium properties of solids and their surfaces. Because the accuracy of the lattice constant is important for estimating oxygen positions and surface dipoles (Sec. 3.2), we used the PBEsol functional [36] as a generalized gradient approximation (GGA) DFT functional and the Heyd–Scuseria–Ernzerhof (HSE) functional for solids (HSEsol) [37] as a hybrid functional. The deviation of the calculated lattice constant of bulk Au from the experimental value (4.070 Å) [28] was 0.01 Å (PBEsol) and 0.02 Å (HSEsol), and that in the previous study [24] was 0.105 Å.

In most experimental studies [1–14,16], the surface orientation was unspecified. We could not identify the surface orientation of the thin films deposited at RT. A mixture of (100) and (111) orientations has been reported for Au films that were sputter-deposited near 500 °C [38], and (100), (101), and (111) surfaces have been studied [2, 3, 6, 13, 15, 23]. Hence, we *ab initio* studied (100), (101), and (111) surfaces.

The partial relaxation (i.e., fixing some atoms at bulk position) and the dipole correction employed in the previous study [24] allow the use of thin unitcells, which occasionally produces artificial results. Instead, we used thick unitcells containing the same number of O-atoms at both top and bottom surfaces and relaxed all the ion positions except for the lattice constants of the slabs. The unitcells in the subsequent part mean slabs, and we also call these unitcells slab unitcells for clarity.

The Monkhorst-Pack k -mesh for Brillouin-zone integration [39] in the geometry relaxation was denser than 24 points per 1 \AA^{-1} . The lattice constant (4.080 \AA) of a bulk Au calculated using PBEsol with a k -mesh $6 \times 6 \times 6$ matched the experimental one, and the properties of BaTiO_3 and SrTiO_3 *ab initio* calculated using PBEsol with k -mesh $6 \times 6 \times 6$ matched experimental ones [40-42]. The inplane lattice constants of the slab unitcells were those of a bulk Au calculated using PBEsol or HSEsol, and the vacuum length of the slab unitcell was 30 \AA . The inplane lattices for (100) surfaces were cuboids (Fig. 2); the unitcells for PBEsol (k -meshes in brackets) were $4.08 \text{ \AA} \times 4.08 \text{ \AA} \times 50 \text{ \AA}$ containing 18 Au atoms ($6 \times 6 \times 1$), $5.77 \text{ \AA} \times 5.77 \text{ \AA} \times 50 \text{ \AA}$ ($4 \times 4 \times 1$) and $8.16 \text{ \AA} \times 4.08 \text{ \AA} \times 50 \text{ \AA}$ ($3 \times 6 \times 1$) containing 36 Au atoms, $8.16 \text{ \AA} \times 8.16 \text{ \AA} \times 50 \text{ \AA}$ containing 72 Au atoms ($3 \times 3 \times 1$), $4.08 \text{ \AA} \times 4.08 \text{ \AA} \times 130 \text{ \AA}$ containing 80 Au atoms ($6 \times 6 \times 1$), and these unitcells contained two or four O atoms.

We define the c -axis as perpendicular to the surface (Fig. 2(c)). The unitcells of (100) surfaces consisted of 9 Au layers along the c -axis (Figs. 2(c) and 2(i)). Additionally, unitcells consisting of 10 layers (20 Au atoms) and 40 layers (80 Au atoms) were tested for consistency. The surfaces of 9 Au layer unitcells are shown in Fig. 2(a), and the top and the bottom surfaces of 10 and 40 Au layer unitcells look like Figs. 2(a) and Fig. 2(b), respectively. The ion positions in Fig. 2(b) completely agree with those in Fig. 2(a) when the ion positions in Fig. 2(b) are translated by $(2.04 \text{ \AA}, 2.04 \text{ \AA}, 0)$.

ϕ of (100) Au surfaces calculated using PBEsol was insensitive to the number of layers (≥ 9); ϕ was 5.189 eV for a 9-layer unitcell (Fig. 2(a)), 5.159 eV for a 10-layer unitcell, and 5.206 eV for a 40-layer unitcell. ϕ of (100) AuO_n surfaces calculated using PBEsol was also insensitive to the number of layers; ϕ of (100) AuO surface was 5.898 eV and 5.887 eV for a 9- and a 10-layer unitcell, respectively. These results suggest the minor importance of Au surface reconstructions, which we neglect.

The inplane lattices of (111) surface were rhombus. The unitcells of (111) surfaces consisted of 10 Au layers containing mostly two O atoms (Fig. 4). The unitcells for PBEsol (k -meshes in brackets) were $2.88 \text{ \AA} \times 2.88 \text{ \AA} \times 50 \text{ \AA}$ containing 10 Au atoms ($9 \times 9 \times 1$), $5.76 \text{ \AA} \times 2.88 \text{ \AA} \times 50 \text{ \AA}$ containing 20 Au atoms ($5 \times 9 \times 1$), $5.76 \text{ \AA} \times 5.76 \text{ \AA} \times 50 \text{ \AA}$ containing 40 Au atoms ($5 \times 5 \times 1$), and $8.64 \text{ \AA} \times 8.64 \text{ \AA} \times 50 \text{ \AA}$ containing 90 Au atoms ($3 \times 3 \times 1$). The unitcells of (101) surfaces consisted of 9 Au layers. The unitcells for PBEsol (k -meshes in brackets) were $2.88 \text{ \AA} \times 4.08 \text{ \AA} \times 42 \text{ \AA}$ containing 9 Au atoms ($9 \times 6 \times 1$) and $5.77 \text{ \AA} \times 4.08 \text{ \AA} \times 42 \text{ \AA}$ containing 18 Au atoms ($4 \times 6 \times 1$).

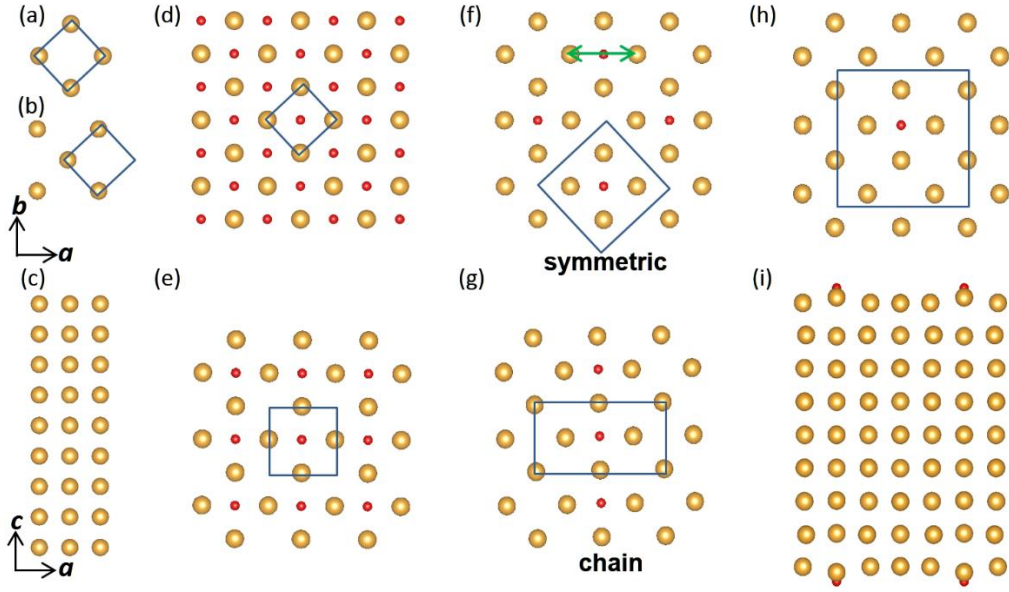


Fig. 2. Top-views ((a), (b), (d)-(g)) and sideviews ((c), (i)) of (100) AuO_n unitcells after relaxation. (a)-(c) Pure Au: (a) surface layer, (b) sub-surface layer, and (c) side view. (d)-(g) surface Au and O. O coverage (occupancy rate) at surface is (d) 100% (AuO), (e) 50% ($\text{AuO}_{1/2}$), (f), (g) 25% ($\text{AuO}_{1/4}$; (f) symmetric and (g) chain), and (h) 12.5% ($\text{AuO}_{1/8}$), (i) side view. Au and O are shown with yellow and red circles. Blue squares show unitcells. A green arrow shows the minimum diagonal surface Au-Au distance surrounding an O atom (d_{AuAu}).

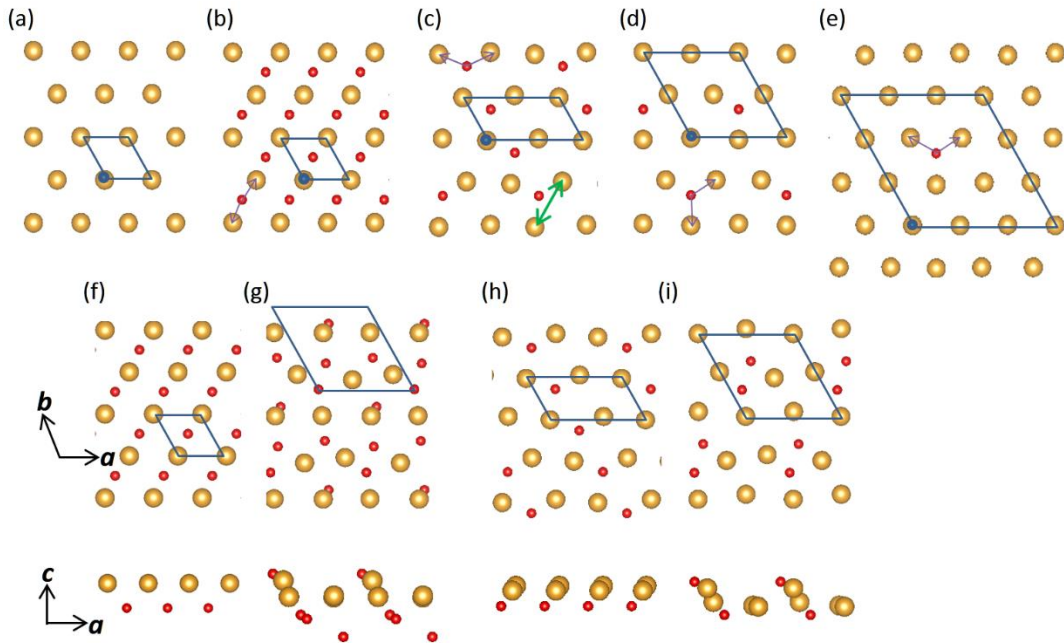


Fig. 3. Top-views and side-views of (111) AuO_n surfaces/subsurface after relaxation. (a) Pure Au. (b)-(e) O-atoms are at surfaces. (f)-(i) O-atoms are at surfaces and subsurfaces, showing top-views and sideviews. O-atom coverage is (b)(f)(g) 100% (AuO), (c)(h)(i) 50% ($\text{AuO}_{1/2}$), (d) 25% ($\text{AuO}_{1/4}$), and (e) 11.1% ($\text{AuO}_{1/9}$). The fraction of subsurface O is (f)(h) 100%, (g) 75%, and (i) 50%. Rhombuses show unitcells. Violet arrows show the distance between O atom and the nearest two Au atoms. A green arrow shows d_{AuAu} .

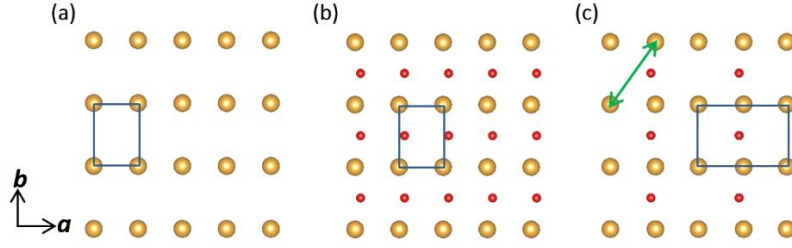


Fig. 4. Top-views of (101) AuO_n surfaces after relaxation. Surface Au and O. (a) Pure Au. O-atom coverage is (b) 100% (AuO), and (c) 50% ($\text{AuO}_{1/2}$). A green arrow shows d_{AuAu} .

These lattice constants were fixed in the geometry relaxation, but all the internal coordinates were relaxed. After relaxation, all the calculated forces were lower than $1 \text{ meV}/\text{\AA}$. The screening parameter (μ) in HSEsol was set to the default value (0.2 \AA^{-1}). The k -grid reduction option of the Hatree-Fock kernel (Nkred) of HSEsol was used. In the benchmark tests, $\text{Nkred} \leq 2$ did not compromise the accuracy of the calculation, and $\text{Nkred} = 2$ was mostly used in the inplane directions. A graphics-processing-unit acceleration [43,44] was employed. Ion positions are visualized using VESTA [45].

The PAW potentials for GGA used in this study are the default ones recommended for metal oxides in the VASP manual: Au PAW potential for gold and O_S PAW potential for oxygen. To ensure better convergence, the Methfessel-Paxton function with a temperature broadening (σ) of 0.05 eV was employed. The calculated values (ϕ 's) using PBEsol ($\sigma = 0.05 \text{ eV}$) with a Methfessel-Paxton and a Gaussian functional were consistent. For example, the Methfessel-Paxton and Gaussian methods resulted in 5.634 eV and 5.634 eV for the $\text{AuO}_{1/4}$ (100) surface and 6.298 eV and 6.305 eV for the $\text{AuO}_{1/2}$ (111) surface, respectively.

The inplane lattices for ion position optimization using HSEsol were those of bulk Au calculated using HSEsol. The lattice constants of a bulk Au obtained using PBEsol (4.080 \AA) and HSEsol (4.090 \AA) were similar. More importantly, ϕ for ion positions optimized with PBEsol and HSEsol was virtually the same; the HSEsol calculations using the ion positions optimized with PBEsol and HSEsol showed that ϕ was 5.177 eV and 5.157 eV for Au (100) surface, respectively, and 5.064 eV and 5.056 eV for Au (101) surface, respectively. Hence, the HSEsol calculations of ϕ of AuO_n ($n > 0$) (100) and (101) surfaces used the ion positions obtained using PBEsol.

In the case of the Au (111) surface, ϕ calculated with HSEsol was 5.460 eV for the ion

positions optimized with PBEsol and 5.227 eV for those optimized with HSEsol. However, this difference (0.23 eV) was negligible as compared with the oxygen-induced variation of ϕ at (111) surface (for $n \geq 1/2$); ϕ changes by >3 eV by oxidation and by >2 eV by the oxygen location such as surface or subsurface (Sec. 3.2). Hence, the calculation of ϕ at the (111) AuO_n ($n > 0$) surface with HSEsol used also the ion positions obtained using PBEsol.

ϕ was sensitive to the electron distribution convergence. In PBEsol calculations, the electron-number convergence (i.e., charge convergence) and the maximum electron density in the major part of the vacuum were $<10^{-6}$ and $<10^{-8} \text{ \AA}^{-3}$, respectively. Although the electron distributions calculated using hybrid functional are considered more accurate than those by PBEsol [36,40-42,46], the electron-number convergence was extremely slow. Hence, the relaxation of the electron distribution was repeated until both electron-number convergences $<5 \times 10^{-5}$ and the maximum electron density around the center of vacuum $<10^{-6} \text{ \AA}^{-3}$ were attained (This required the energy convergence $<0.01\text{--}0.1$ neV).

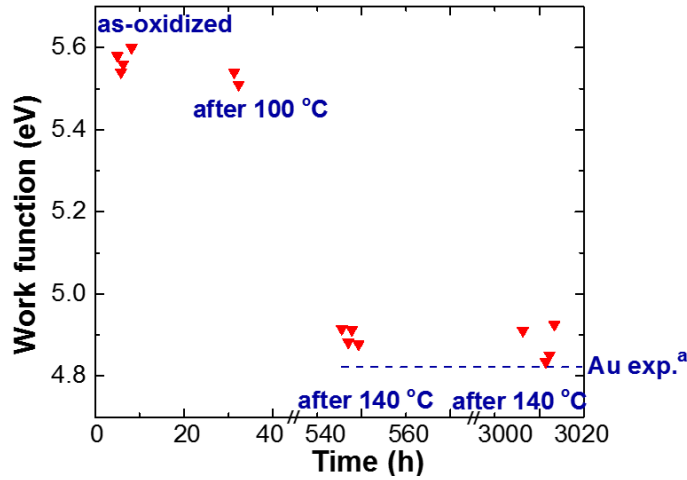


Fig. 5. Change in work function (ϕ) of O-atom-irradiated Au surface with time and annealing in UHV. The average ϕ of the as-oxidized surface (at 5–8.2 h) is 5.72 eV. ^a ref. [49]. ^b ref. [50].

3. Results and discussion

We introduce notations for specific work functions

$$\phi(X)_S \quad (X = \text{Au or AuO}_n \ (n > 0), S = 001, 101, \text{ or } 111),$$

to specify the surface composition (X) and the surface orientation (S). Additionally, we define

$$\Delta\phi(X)_S \equiv \phi(X)_S - \phi(\text{Au})_S$$

to express the change in ϕ of a given surface orientation. When the surface composition or orientation is unspecified, X or S is omitted. For instance, $\phi(\text{AuO}_n)$ and $\Delta\phi(\text{AuO}_n)$ denote $\phi(\text{AuO}_n)_S$ and $\Delta\phi(\text{AuO}_n)_S$ of any surface orientation. $\Delta\phi$ denotes $\Delta\phi(X)_S$ of any X and any S .

3.1. Experimental results

ϕ of the KPFM probe that was a very heavily-doped clean n-type Si (ϕ_{Si}) corresponds to the energy level of the conduction band bottom of Si, which is 4.05–4.15 eV [17,47,48]. In our subsequent analysis, we use $\phi_{\text{Si}} = 4.15$ eV [47] because. ϕ was estimated as $\phi = \phi_{\text{Si}} - \phi_{\text{KPFM}}$, where ϕ_{KPFM} is a surface potential given by KPFM.

The reported experimental ϕ of Au thin films is 4.83 eV measured using a Kelvin method [49] and 5.1 ± 0.1 eV measured using a photoemission method [50], while the surface orientation was not specified. The difference between the two values was attributed to the quality of the vacuum used for the Au deposition [50]. Since the quality of the vacuum used for the deposition in this paper was between those of refs [49, 50], we use an average $\phi(\text{Au}) = -4.965$ eV.

All experiments in Fig. 5 were conducted in the main UHV chamber. The sample underwent one short heating cycle up to 100 °C for 10 min, followed by two cycles of heating up to 140 °C heating, with the duration of >100°C being 1 hour. In Fig. 5, ϕ was 5.57 eV on average in an as-transferred state experiencing no heating, and almost unchanged after the short 100 °C heating (5.53 eV on average). After the 1st 140 °C heating, ϕ decreased to 4.88 eV on average but was unchanged by the 2nd 140 °C heating (4.90 eV on average).

The experiments by Krozer and Rodah [51], Tsai et al. [52], and Ono and Cuenya [53] suggest that 150 °C in UHV decomposes Au oxides at surfaces to yield Au. Figure 5 shows that the ϕ value after heating to 140°C closely matches the reported experimental $\phi(\text{Au})$ [49], indicating that the surface after the 2nd 140 °C heating was predominantly Au. This is further supported by the observed change in ϕ by the 140°C heating that agreed with that of oxidized Au reported by Saliba et al. [15] and Gottfried et al. [23].

3.2. *Ab initio* results

3.2.1 Work function, binding energy, and structures

The DFT calculations by Sun et al. [18] and Daigle and BelBruno [22] show that the binding energy is maximized when O resides at hole sites surrounded by Au atoms (Figs. 2-4) and does not depend much on the orientation of the surface. Hence, we investigated (100), (111), and (101) surfaces having O-atoms at hole sites, with varying O-atom coverages (i.e., occupancy rate); we also started the geometry relaxation with O-atoms outside hole sites and found that the final location was at hole sites. Figures 2-4 show Au, AuO, AuO_{1/2}, AuO_{1/4}, and AuO_{1/8} (100) surfaces, Au, AuO, AuO_{1/2}, AuO_{1/4}, and AuO_{1/9} (111) surfaces/subsurfaces, and Au, AuO, and AuO_{1/2} (101) surfaces after relaxation.

The surface formation energy of the (100), (111), and (101) surfaces was 1.1 eV, 0.3eV, and 0.8 eV, respectively. These values indicate that the Au (111) surface was the most stable, which is consistent with the experiment on a freestanding Au film [54]. The surface formation energy slightly decreased as the size of the slabs increased; for the (100) surface, it was 1.1 eV for the slabs with 9 or 10 Au layers and 0.7 eV for the slabs with 40 Au layers.

The stable O position at the (100) surfaces in Fig. 2 was near the center of surrounding Au atoms. The stable O position at the (111) surfaces can be described by the two distances from the two nearest Au atoms (Fig. 3); the distances at AuO, AuO_{1/2}, AuO_{1/4}, and AuO_{1/9} (111) surfaces were 1.995 Å and 1.995Å, 2.068 Å and 2.092Å, 2.094 Å and 2.094 Å, and 2.116 Å and 2.120 Å, respectively.

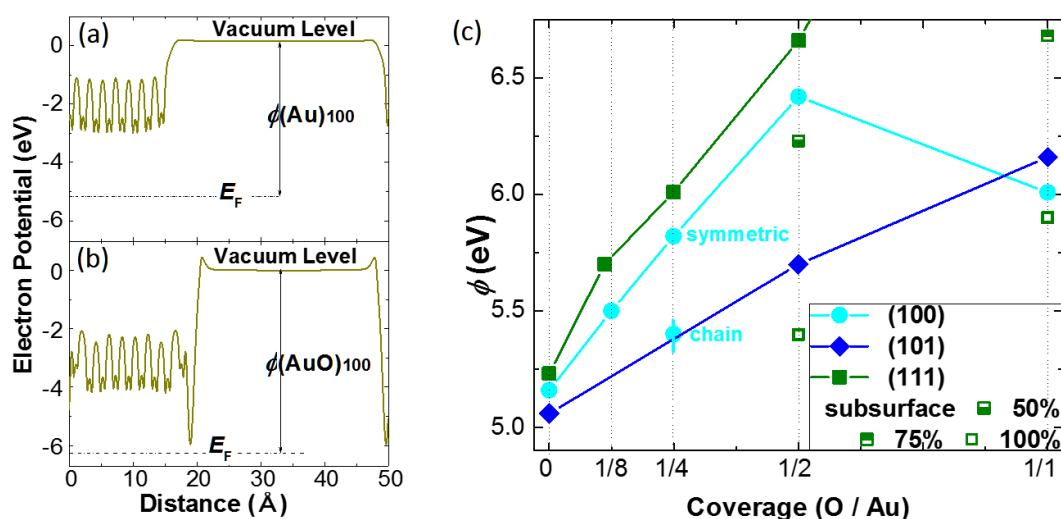


Fig. 6. Potential distribution in (a) Au and (b) AuO slab unitcells (HSEsol). (c) ϕ vs. O coverage (occupancy rate). 50%, 75%, and 100% represent the fraction of subsurface O atoms (Figs. 3(f)-3(i)); otherwise, the subsurface O atoms are 0. Light blue circles with and without a bar represent the symmetric and chain O distributions shown in Figs. 2(f) and 2(g), respectively

ϕ is the energy required to move an electron from the Fermi level to the vacuum level [17] and is associated with the dipole-like charge distribution at the surface. In metals, this charge distribution is caused by the quantum mechanical tunneling leakage of electrons (Fig. 6(a)). Further, at the oxide surfaces, the effect of ion charge density overrides, causing an increase in ϕ . This increase is visible as the enhancement of the peaks of ϕ at the surfaces (Fig. 6(b)).

ϕ calculated using PBEsol and HSEsol is listed in Table 1. Because HSEsol generally provides more accurate electronic properties than DFT [40-42], all the figures of ϕ use HSEsol results except for Appendix. The value in ref. [50] is appropriate for the comparison with theories because the Au film in ref. [50] is considered to be purer than ref. [49].

Coverage (eV)	HSEsol			PBEsol			ref.[24]
	(100)	(101)	(111)	(100)	(101)	(111)	
0 (Au)	5.16	5.06	5.23	5.19	5.12	5.27	5.28
1/8 symmetric	5.50		5.71	5.47		5.63	5.57
1/4 chain	5.40			5.42			
1/4	5.82		6.01	5.63		5.79	5.82
1/2	6.42	5.72	6.66	6.01	5.62	6.30	6.17
1/2 subsurface 50%			6.25			6.02	
1/2 subsurface 100%			5.40			5.31	
1	6.01	6.16	8.54	5.80	6.01	8.24	7.95
1 subsurface 75%			6.68			6.26	
1 subsurface 100%			5.90			5.86	

Table 1. Work function (eV) calculated using HSEsol and PBEsol. Ref. [24] (PW91) and PBEsol are GGA-DFT. Experimental ϕ (Au) is 4.83 eV [49] and 5.1±0.1 eV [50].

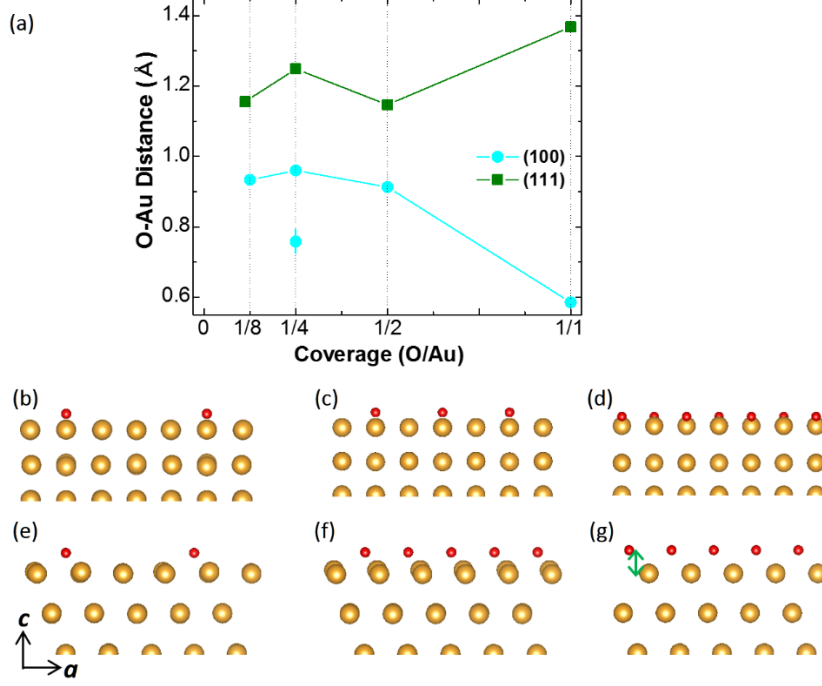


Fig. 7. Height of O from the 1st Au layer ($h^{\text{O-Au}}$). (b)-(g) (100) surface side-views. (e)-(g) (111) surfaces side-views. (b) AuO_{1/8}, (c) AuO_{1/2}, (d) AuO, (e) AuO_{1/9}, (f) AuO_{1/2}, (g) AuO. Green arrow shows $h^{\text{O-Au}}$.

Figure 6(c) shows $\phi(\text{Au})_{111} > \phi(\text{Au})_{001} > \phi(\text{Au})_{101}$. This difference may be a cause of the variation in reported ϕ of polycrystalline Au thin films, in addition to the difference in vacuum level suggested by Eastman [50]. In Table 1, PBEsol slightly overestimates $\phi(\text{Au})$ and underestimates $\phi(\text{AuO}_n)$ compared to HSEsol, which is in line with the calculations of $\phi(\text{Au})_{111}$ using PBE (GGA-DFT) and HSE (hybrid) functionals by Yoo et al. [55]. Hence, the change in ϕ with oxygen-chemisorption estimated using PBEsol or GGA [24] is smaller than that calculated using HSEsol. Table 1 shows that $\phi(\text{Au})_{111}$ and $\Delta\phi(\text{AuO}_n)_{111}$, calculated using PBEsol, match $\Delta\phi(\text{AuO}_n)_{111}$ reported by Shi and C. Stampfl [24].

In Table 1 and Fig. 6(c), $\phi(\text{AuO})_{001}$ is unexpectedly smaller than $\phi(\text{AuO}_{1/2})_{001}$, and $\phi(\text{AuO}_{1/4})_{001}$ (chain) is smaller than $\phi(\text{AuO}_{1/2})_{001}$ (symmetric). Additionally, $\phi(\text{AuO}_n)_{111}$ increases more rapidly with O-coverage (n) than $\phi(\text{AuO}_n)_{001}$.

As one of the origins of these observations, we note that the dipole due to O-atoms increases with the height of O from the topmost Au layer ($h^{\text{O-Au}}$) and contributes to ϕ . $h^{\text{O-Au}}$ in Fig. 7(a) exhibits a

good correlation with $\phi(\text{AuO}_n)_{001}$ and $\phi(\text{AuO}_n)_{111}$ (Fig. 6(c)); the definition of $h^{\text{O-Au}}$ is shown by an arrow in Fig. 7(g).

Specifically, $h^{\text{O-Au}}$ at the AuO (100) surface is shorter than $h^{\text{O-Au}}$ at AuO_{1/2} (100) surface (Fig. 7(d) vs. Fig. 7(c)). $h^{\text{O-Au}}$ is longer at AuO_n (111) surfaces than at the AuO_n (100) surfaces (Figs. 7(b)-7(d) vs. Figs. 7(e)-7(g)). At the AuO_{1/4} (100) surface, $h^{\text{O-Au}}$ is shorter in a chain-like O-configuration than in a symmetric O-configuration (Fig. 7(a)). In the case of the (101) surface, $\phi(\text{AuO}_n)_{101}$ correlated only weakly with $h^{\text{O-Au}}$.

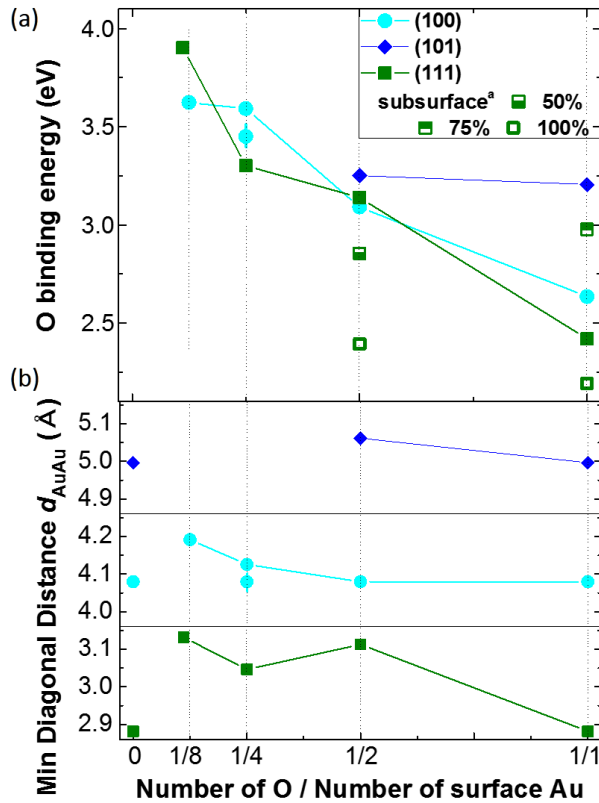


Fig. 8. (a) O-atom binding energy vs. O-atom coverage. (b) d_{AuAu} vs. O-atom coverage. d_{AuAu} of (100) and (111) surface is defined by the green arrow in Figs. 2(f), 3(c), and 4(c). ^a Figs. 3(f)-3(i)

The binding energy of O-atom was comparable with those reported by Sun et al. [18] and Daigle and BelBruno [22]. The binding energy of both (111) and (100) surfaces rapidly decreased with the increase in coverage (Fig. 8(a)), agreeing with the results of Shi and Stampfl [24] on the (111) surface.

These observations are attributed to the difficulty in the changes of Au atom positions surrounding each O-atom to accommodate the O-atoms (Fig. 8(b)). This also explains the $h^{\text{O-Au}}$ (height

of O) in Fig. 7. Accordingly, Fig. 8(b) shows that the distance between surface Au atoms surrounding an O-atom, d_{AuAu} , decreases as O-atom coverage increases. The *ab initio* calculations in this paper fixed the inplane lattice constants of the slab unitcells; this situation corresponds to thin films on substrates and bulk materials. In this case, the local expansion of d_{AuAu} is expected to become difficult as the coverage increases.

In particular, d_{AuAu} at AuO surface is the same as d_{AuAu} at Au surface because all Au atoms are next to O atoms. This restriction is expected to reduce on Au nanoparticles and at elevated temperatures. Such reduction can be the origin of the high reactivity of nano Au particles [12]. Additionally, Fig. 8(a) suggests that O atoms with scarce coverage can persist because the energy gained by the chemisorption increases with the decreasing coverage.

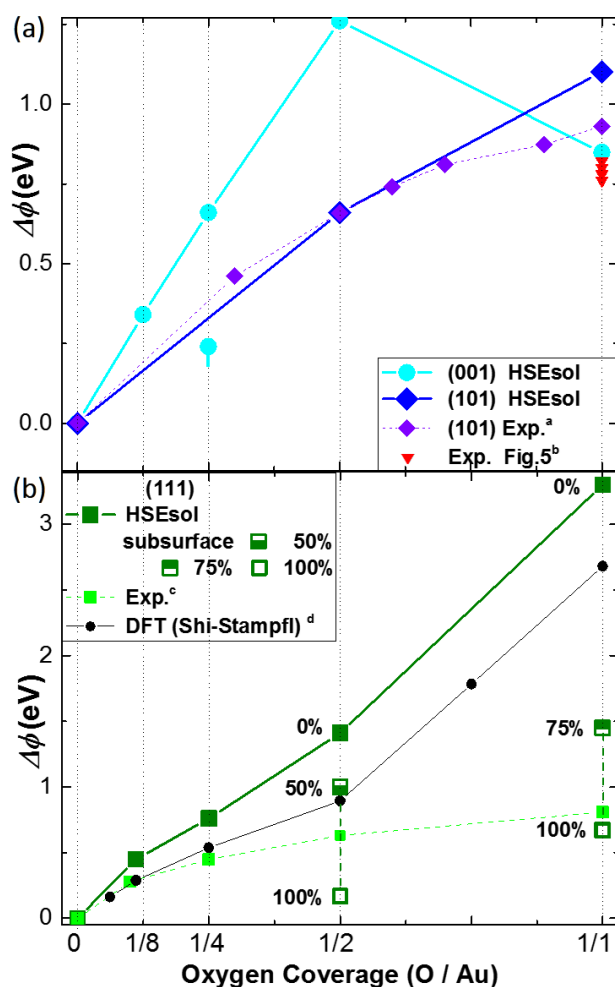


Fig. 9. Change of work function $\Delta\phi$ vs. coverage and comparison with experiments. (a) (100) and (101). (c) (111). ^a Gottfried et al. [23]. ^b Difference between $\phi(\text{Au})$ [49] and ϕ of an as-oxidized surface (at 5–8.2 h) in Fig. 5. ^c Saliba et al. [15]. ^d Shi and C. Stampfl [24].

3.2.2 Comparison of $\Delta\phi$ with experiments

Figure 9 displays $\Delta\phi$ vs. coverage and compares the HSEsol results with the experiments in Fig. 5 and the reported experimental results. $\Delta\phi(\text{AuO}_n)_{101}$ calculated using HSEsol agrees with the experiments of (101) Au surface by Gottfried et al. [23]. In Sec. 3.1, the O-atom coverage at the as-oxidized surface in Fig. 5 was shown to be 100%, and the $\Delta\phi$ of this surface (≈ 0.8 eV) matched $\Delta\phi(\text{AuO})_{001}$ calculated using HSEsol. We note that the BaTiO_3 substrate favors the formation of (100) oriented Au films, because of the experiments by Mader et al. [54]. Further, $\Delta\phi$ in Fig. 5 is consistent with the reported experimental $\Delta\phi(\text{AuO})_{101}$ and $\Delta\phi(\text{AuO})_{111}$ (≈ 0.8 – 0.9 eV) [15, 23].

Contrastingly, these experimental values are inconsistent with the theoretical $\Delta\phi(\text{AuO}_n)_{111}$ (Table 1); e.g., both present and reported calculations [24] of $\Delta\phi(\text{AuO})_{111}$ (≈ 3 eV) completely contradict the experimentally observed $\Delta\phi(\text{AuO})_{111} \approx 0.8$ eV. To explain this, the low energy electron diffraction (LEED) results by Saliba et al. [15] are indicative; LEED shows noticeable disorder at the surface for O-atom coverage $\geq 50\%$ at the (111) surface. Further, the correlation of $\phi(\text{AuO}_n)$ with $h^{\text{O-Au}}$ (Fig. 6(c) vs. Fig. 7(a)) suggests that a reduced or negative $h^{\text{O-Au}}$ may be the cause of the experimentally observed small ϕ .

3.2.3 Au (111) surface/subsurface

Hence, we calculated the Au (111) surface where O atoms are located at the surface and the subsurface and observed disordered Au and O as shown in Figs. 3(f) and 3(g). These disorders are noticeable in the vertical directions, leading to an increased spacing between the surface and subsurface Au layers.

The top views in Figs. 3(f) and 3(g) illustrate that O-atoms can penetrate the subsurface from the vacuum without disturbing surface Au atoms. Consistent with Shi and Stampfl [24], the binding energy decreased when all the O-atoms existed in the subsurface only. However, contrary to the report by Shi and Stampfl [24], the decrease in the binding energy was small. Moreover, we found that the binding energy for 100% coverage increased when the O-atoms existed at both surface and subsurface (Fig. 8(a)). We attribute these differences between the present and reported results [24] to the partial relaxation of ion positions in ref. [24] and the full relaxation of ion positions in this study.

When a part of O atoms was on the subsurface, ϕ decreased significantly (Table 1 and Fig. 9). In the subsequent part of this paragraph, we will focus on the (111) surface with 100% O-atom coverage. The percentage in the parentheses in the next paragraph represents the fraction of O atoms located at the subsurface, e.g., $\Delta\phi(\text{AuO}_n)_{111}[100\%]$.

Specifically, HSE calculations showed that $\Delta\phi(\text{AuO})_{111}[75\%]$ was 0.64 eV higher than the experimental $\Delta\phi(\text{AuO})_{111}$ [15] and $\Delta\phi(\text{AuO})_{111}[100\%]$ was 0.1 eV lower than the experimental $\Delta\phi(\text{AuO})_{111}$ [15] (Fig. 9). Hence, the HSE calculation with a coverage between 75% and 100% can accurately replicate the experimental $\Delta\phi$ [15]. Similar results are obtained using PBEsol (Appendix).

3.2.4 Uniqueness of Au (111) surface

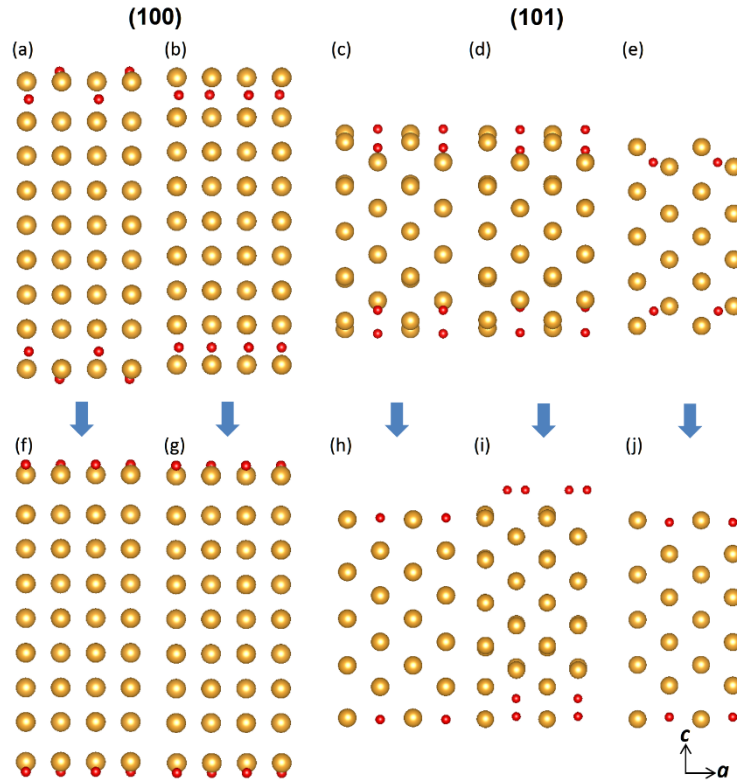


Fig. 10. Side-views: Initial and final positions of O-atoms at (100) and (101) subsurface. (a)-(e) initial ion positions. (b), (e) all atoms at subsurface. (a), (c), (d) 50% O atoms at subsurface. Subsurface O-atoms in (c) are located more inwards than those in (d). (f)-(g) final ion positions after relaxation.

These properties of the (111) Au surface were special; in case of (100) and (101) Au surface, O-atoms were unstable at the subsurface. When we optimized the ion positions, the O atoms that were initially placed at subsurface (Figs. 10(a)-10(e)) moved to surface after relaxation (Figs. 10(f)-10(h) and Fig.10(j)). The binding energy of O atoms in Fig. 10(i) was smaller than that of Fig. 10(i).

3.2.5 Density of states

The electronic properties at the surface are crucial for STM studies of chemisorbed O atoms, as shown by Xu et al. [2]. In Fig. 11, the local density of states (LDOS) at E_F on Au surfaces increased with the density of Au atoms at the surface and was the highest at the (111) surface and the lowest at the (101) surface. Chemisorbed O atoms changed LDOS near the surfaces (Fig. 11), leading to a reduction in metallicity. This reduction was most significant at the (101) surface, where the metallicity was nearly vanishing.

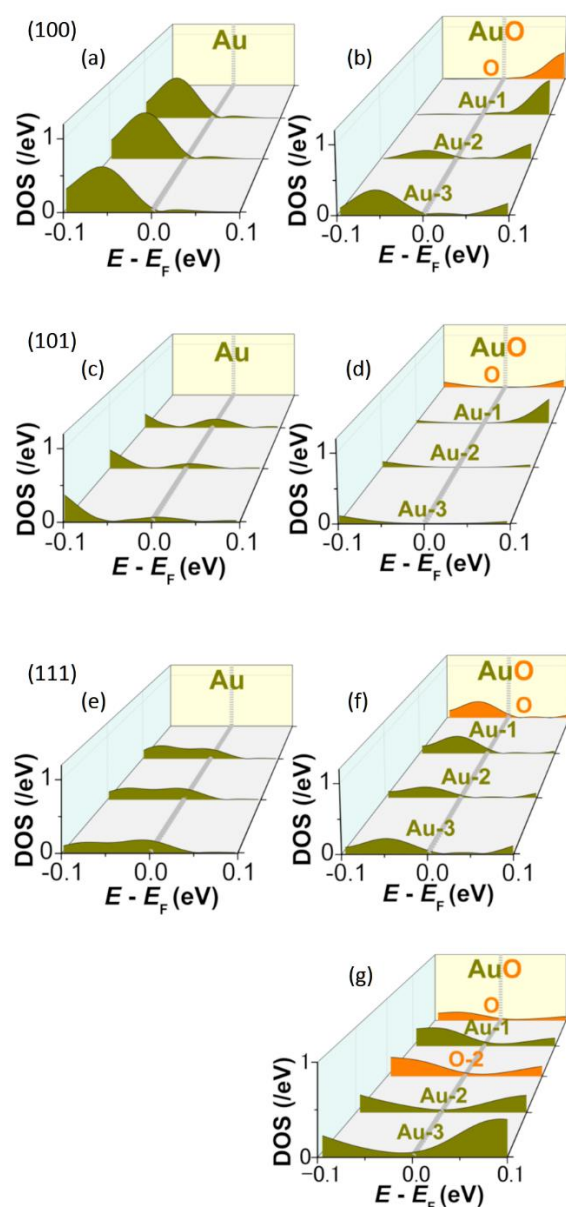


Fig. 11. LDOS at Au and AuO surfaces (calculated using HSEsol). (a)(b) (100), (c)(d) (101), and (e)-(g) (111). Au-1, Au-2, and Au-3 denote the LDOS of Au at the top, the 2nd top, 3rd top surface. O and O-2 denote the LDOS of O above the top Au surface and O between the top and the 2nd top Au surface.

4. Summary

ϕ (work function) and structures of oxygen chemisorbed (100), (101), and (111) Au surfaces with various levels of O-atom coverage (n) were *ab initio* calculated using DFT (PBEsol) and hybrid functional (HSEsol). The calculations accurately reproduced the experimental lattice constants of bulk Au. $\phi(\text{Au})_{001}$ (ϕ at (100) Au surface), $\phi(\text{Au})_{101}$, and $\phi(\text{Au})_{111}$ calculated using the hybrid functional was 5.16 eV, 5.06 eV, and 5.23 eV, respectively, and consistent with the experimental ϕ of polycrystalline Au films (5.1 ± 0.1 eV) [50].

$\Delta\phi(\text{AuO}_n)_{101}$ (the difference between $\phi(\text{AuO}_n)_{101}$ and $\phi(\text{Au})_{101}$), calculated using HSEsol, matched the experiments by Gottfried et al. [23]. The as-oxidized surface of the Au surface in the experiments of Fig. 5 was considered to be AuO.

In the present experiment and the reported experiments on (111) and (101) surfaces [15,23], $\Delta\phi(\text{AuO})$ was 0.8–0.9 eV (Fig.9). This value was in line with the present HSEsol calculations on (100) and (101) surfaces but contradicted both the present and previous calculations [24] of $\Delta\phi$ (3 eV) at the (111) surfaces. This contradiction was resolved; we found that when O atoms are at (111) surface and subsurface, the theoretical $\Delta\phi$ at (111) agrees with experimental $\Delta\phi$ (0.8–0.9 eV). This state is considered to correspond to the experiments, because the oxygen-chemisorption is more stable in this state than when O atoms are at (111) surface only (contrary to the previous calculation [24]). This finding aligned with the observations of disorders found by Saliba et al. [15] and the stability (i.e., binding energy) in Fig. 8(a). The stability of O-atoms at the subsurface was unique to the (111) surfaces; the stability was not observed at the (100) and (101) subsurfaces.

The chemisorption of O changed the Au-lattices at the surface (Fig. 8(b)), which was noticeable on the (111) Au surface. As a result, the energy gains from the chemisorption decreased as coverage increased (Fig. 8(a)). Because the deformation energy of Au lattices is expected to reduce on the surface of nanoparticles, it is anticipated that the chemisorption of O is easier on Au nanoparticles than on bulk Au. This trend is not limited to O, suggesting that Au nanoparticles [12] and atomically coarse surfaces are more reactive than bulk Au. $\phi(\text{AuO}_n)$ can be useful for obtaining band diagrams experimentally because Au films are used as standard electrodes and serve as a reference of ϕ [17].

Acknowledgements

This work was supported by Murata Science Foundation and KAKENHI Grant No. JP19K21853. The discussions with P. Blöchel of TU Clausthal is greatly acknowledged.

Declaration of competing interest The author declares no competing interest.

Data Availability

The data in my manuscript can be obtained from the corresponding author upon reasonable request.

APPENDIX

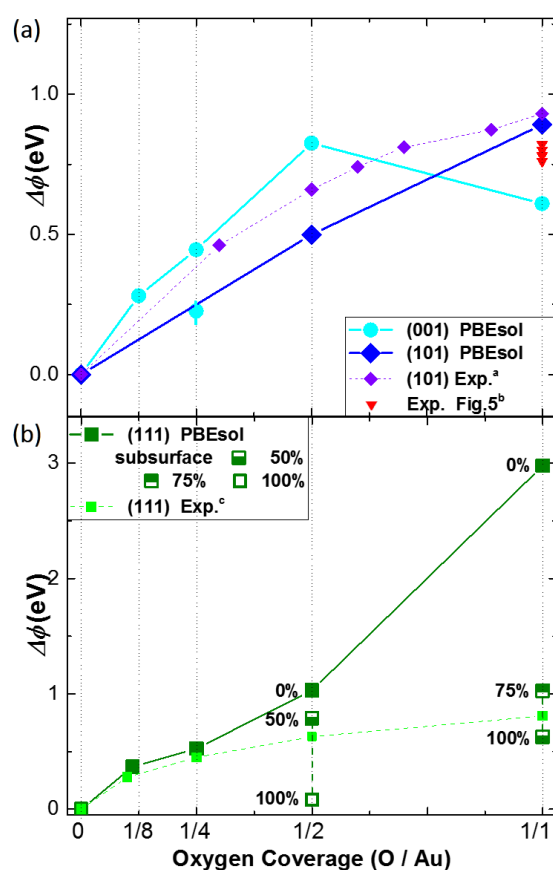


Fig. 12. Change of work function $\Delta\phi$ vs. coverage and comparison with experiments. The theoretical data were calculated using PBEsol instead of HSEsol (Fig. 9). ^a ref. [23]. ^b Difference between $\phi(\text{Au})$ [49] and ϕ of an as-oxidized surface in Fig. 5. ^c ref. [15]. HSEsol results agree better with experiments than PBEsol results.

References

1. D. M. Mattox, Influence of oxygen on the adherence of gold films to oxide substrates, J. Appl. Phys. 37, 3613 (1966). <https://doi.org/10.1063/1.1708913>
2. F. Xu, I. Fampiou, C. R. O'Connor, S. Karakalos, F. Hiebel, E. Kaxiras, R. J. Madix and C. M. Friend, Water facilitates oxygen migration on gold surfaces, Phys. Chem. Chem. Phys. 20, 2196 (2018),

<https://doi.org/10.1039/C7CP06451A>

3. O. Diaz-Morales, F. Calle-Vallejo, C. de Munck, and M. T. M. Koper, Electrochemical water splitting by gold: evidence for an oxide decomposition mechanism, *Chem. Sci.*, 4, 2334 (2013).
<https://doi.org/10.1039/C3SC50301A>
4. H. A. Laitinen and M. S. Chao, The anodic surface oxidation of gold, *J. Electrochem. Soc.*, 108, 726 (1961).
DOI: 10.1149/1.2428206
5. S. B. Brummer and A. C. Makrides, Surface oxidation of gold electrodes, *J. Electrochem. Soc.*, 111, 1122 (1964). DOI: 10.1149/1.2425933
6. H. Angerstein-Kozłowska, B. E. Conway, A. Hamelin, and L. Stoicoviciu, Elementary Steps of Electrochemical Oxidation of Single-crystal Planes of Gold - I. Chemical Basis of Processes Involving Geometry of Anions and the Electrode Surfaces, *Electrochim. Acta.*, 31, 1051 (1986).
[https://doi.org/10.1016/0013-4686\(86\)80020-2](https://doi.org/10.1016/0013-4686(86)80020-2)
7. J. J. Pireaux, M. Liehr, P. A. Thiry, J. P. Delrue, and R. Caudano, Electron spectroscopic characterization of oxygen adsorption on gold surfaces II. Production of gold oxide in oxygen DC reactive sputtering, *Surf. Sci.* 141, 221 (1984). [https://doi.org/10.1016/0039-6028\(84\)90207-3](https://doi.org/10.1016/0039-6028(84)90207-3)
8. G. Tremiliosi-Filho, L. H. Dall'Antonia, and G. Jerkiewicz, Limit to extent of formation of the quasi-two-dimensional oxide state on Au electrodes, *J. Electroanal. Chem.*, 422, 149 (1997).
[https://doi.org/10.1016/S0022-0728\(96\)04896-6](https://doi.org/10.1016/S0022-0728(96)04896-6)
9. S. J. Xia and V. I. Birss, A Multi-technique study of compact and hydrous Au oxide growth in 0.1 m sulfuric acid solutions, *J. Electroanal. Chem.*, 500, 562 (2001). [https://doi.org/10.1016/S0022-0728\(00\)00415-0](https://doi.org/10.1016/S0022-0728(00)00415-0)
10. P. Fuchs, Low-pressure plasma cleaning of Au and PtIr noble metal surfaces, *Appl. Surf. Sci.*, 256, 1382 (2009). <https://doi.org/10.1016/j.apsusc.2009.08.093>
11. A. Y. Klyushin, T. C. R. Rocha, M. Hävecker, A. Knop-Gericke, and R. Schlögl, A near ambient pressure XPS study of Au oxidation, *Phys. Chem. Chem. Phys.*, 16, 7881 (2014).
<https://doi.org/10.1039/c4cp00308j>
12. D. C. Lim, I. Lopez-Salido, R. Dietsche, M. Bubek, and Y. D. Kim, Oxidation of Au nanoparticles on HOPG using atomic oxygen, *Surf. Sci.* 600, 507 (2006). <https://doi.org/10.1016/j.susc.2005.10.064>
13. D. Dickertmann, J.W. Schultze, K.J. Vetter, Electrochemical formation and reduction of monomolecular oxide layers on (111) and (100) planes of gold single crystals, *J. Electroanal. Chem. Interfacial Electrochem.* 55, 429 (1974). [https://doi.org/10.1016/S0022-0728\(74\)80437-7](https://doi.org/10.1016/S0022-0728(74)80437-7)
14. R. G. P. Giron and G. S. Ferguson, Interfacial redox properties of gold/gold oxide in the presence and absence of applied potential, *J. Electrochem. Soc.* 166, H47-H53 (2019). DOI: 10.1149/2.0931902jes
15. N. Saliba, D. H. Parker, and B. E. Koel, Adsorption of oxygen on Au(111) by exposure to ozone, *Surf. Sci.*, 410, 270 (1998). [https://doi.org/10.1016/S0039-6028\(98\)00309-4](https://doi.org/10.1016/S0039-6028(98)00309-4)
16. N.D.S. Canning, D. Outka, R.J. Madix, The adsorption of oxygen on gold, *Surf. Sci.* 141, 240 (1984).
[https://doi.org/10.1016/0039-6028\(84\)90209-7](https://doi.org/10.1016/0039-6028(84)90209-7)
17. S.M. Sze and K. Ng Kwok, *Physics of Semiconductor Devices* (John Wiley & Sons, New York 2007).
DOI:10.1002/0470068329
18. K. Sun, M. Kohyama, S. Tanaka, and S. Takeda, Theoretical study of atomic oxygen on gold surface by Hückel theory and DFT calculations, *J. Phys. Chem. A*, 116, 38, 9568 (2012). <https://doi.org/10.1021/jp306906j>
19. R. Liu, Adsorption and dissociation of H₂O on Au (1 1 1) surface: A DFT study, *Comput. Theor. Chem.* 1019, 141 (2013). <https://doi.org/10.1016/j.comptc.2013.07.009>

20. Z. Jiang, M. Li, T. Yan, T. Fang, Decomposition of H₂O on clean and oxygen-covered Au (1 0 0) surface: A DFT study, *Appl. Surf. Sci.* 315, 16 (2014). <https://doi.org/10.1016/j.apsusc.2014.07.076>
21. R.-P. Ren, L. Cheng, Y.-K. Lv, Selective oxidation of vinyl chloride on Ag₂O(100), Cu₂O(100), and Au₂O(100) surfaces: A density functional theory study, *Surf. Sci.* 630, 116 (2014). <https://doi.org/10.1016/j.susc.2014.06.006>
22. A. D. Daigle and J. J. BelBruno, Density functional theory study of the adsorption of oxygen atoms on gold (111), (100) and (211) surfaces, *Surf. Sci.* 605 1313 (2011) <https://doi.org/10.1016/j.susc.2011.04.025>
23. J.M. Gottfried, K.J. Schmidt, S.L.M. Schroeder, K. Christmann, Oxygen chemisorption on Au-(1×2) II. Spectroscopic and reactive thermal desorption measurements, *Surf. Sci.* 525, 197 (2003). [https://doi.org/10.1016/S0039-6028\(02\)02559-1](https://doi.org/10.1016/S0039-6028(02)02559-1)
24. H. Shi and C. Stampfl, First-principles investigations of the structure and stability of oxygen adsorption and surface oxide formation at Au(111), *Phys. Rev. B.* 76, 075327 (2007). <https://doi.org/10.1103/PhysRevB.76.075327>
25. Ch. Sommerhalter, Th. W. Matthes, Th. Glatzel, A. Jäger-Waldau, and M. Ch. Lux-Steiner, High-sensitivity quantitative Kelvin probe microscopy by noncontact ultra-high-vacuum atomic force microscopy, *Appl. Phys. Lett.* 75, 286 (1999). <https://doi.org/10.1063/1.124357>
26. R. Tran, X.-G. Li, J. H. Montoya, D. Winston, K. A. Persson, and S. P. Ong, Anisotropic work function of elemental crystals, *Surf. Sci.* 687, 48 (2019). <https://doi.org/10.1016/j.susc.2019.05.002>
27. S. De Waele, K. Lejaeghere, M. Sluydts, and S. Cottenier, Error estimates for density-functional theory predictions of surface energy and work function, *Phys. Rev. B* 94, 235418 (2016). <https://doi.org/10.1103/PhysRevB.94.235418>
28. E. R. Jette and F. Foote, Precision determination of lattice constants, *J. Chem. Phys.* 3, 605 (1935). <https://doi.org/10.1063/1.1749562>
29. T. Nakatani, A. Yoshiasa, A. Nakatsuka, T. Hiratoko, T. Mashimo, M. Okube and S. Sasaki, Variable-temperature single-crystal X-ray diffraction study of tetragonal and cubic perovskite-type barium titanate, *Acta Cryst.* 72, 151 (2016). <https://doi.org/10.1107/S2052520615022544>
30. N. Terada, S. Kashiwaya, H. Takashima, S. Ueno, M. Koyanagi, and H. Ihara, Control of surface electronic structure of high T_C superconducting films for Josephson junctions and electron spectroscopy, *IEEE Trans. Appl. Supercond.* 9, 1704-1707(1999). <https://doi.org/10.1109/77.784781>
31. T. Shimizu and H. Okushi, Intrinsic electrical properties of Au/SrTiO₃ Schottky junctions *J. Appl. Phys.* 85, 7244 (1999). <https://doi.org/10.1063/1.370539>
32. P. E. Blöchl, Projector augmented-wave method. *Phys. Rev. B* 50, 17953–17979 (1994). <https://doi.org/10.1103/PhysRevB.50.17953>
33. G. Kresse and J. Hafner, Ab initio molecular dynamics for liquid metals. *Phys. Rev. B* 47, 558R (1993). <https://doi.org/10.1103/PhysRevB.47.558>
34. G. Kresse and J. Furthmüller, Efficiency of ab-initio total energy calculations for metals and semiconductors using a plane-wave basis set. *Comput. Mater. Sci.* 6, 15 (1996). [https://doi.org/10.1016/0927-0256\(96\)00008-0](https://doi.org/10.1016/0927-0256(96)00008-0)
35. G. Kresse and D. Joubert, From ultrasoft pseudopotentials to the projector augmented-wave method. *Phys. Rev. B* 59, 1758 (1999). <https://doi.org/10.1103/PhysRevB.59.1758>

36. J. P. Perdew, A. Ruzsinszky, G. I. Csonka, O. A. Vydrov, G. E. Scuseria, L. A. Constantin, X. Zhou, and K. Burke, Restoring the density-gradient expansion for exchange in solids and surfaces. *Phys. Rev. Lett.* 100, 136406 (2008). <https://doi.org/10.1103/PhysRevLett.100.136406>
37. L. Schimka, J. Harl, and G. Kresse, Improved hybrid functional for solids: The HSEsol functional, *J. Chem. Phys.* 134, 024116 (2011). <https://doi.org/10.1063/1.3524336>
38. S. Nakao, K. Saitoh, M. Ikeyama, H. Niwa, S. Tanemura, Y. Miyagawa, S. Miyagawa, Preparation of thin gold films by the forward-sputtering method, *Surface and Coatings Technology* 66, 464 (1994). [https://doi.org/10.1016/0257-8972\(94\)90050-7](https://doi.org/10.1016/0257-8972(94)90050-7)
39. H. J. Monkhorst and J. D. Pack, Special points for Brillouin-zone integrations, *Phys. Rev. B* 13, 5188 (1976). <https://doi.org/10.1103/PhysRevB.13.5188>
40. R. Wahl, D. Vogtenhuber, and G. Kresse, SrTiO₃ and BaTiO₃ revisited using the projector augmented wave method: Performance of hybrid and semilocal functionals, *Phys. Rev. B* 78, 104116 (2008). <https://doi.org/10.1103/PhysRevB.78.104116>
41. Y. Watanabe, Calculation of strained BaTiO₃ with different exchange correlation functionals examined with criterion by Ginzburg-Landau theory, uncovering expressions by crystallographic parameters, *J. Chem. Phys.* 148, 194702 (2018). <https://doi.org/10.1063/1.5022319>
42. Y. Watanabe, DFT + U accurate for strain effect and overall properties of perovskite oxide ferroelectrics and polaron, *J. Appl. Phys.* 135, 224103 (2024) <https://doi.org/10.1063/5.0213487>
43. M. Hacene, A. A. Sedrakian, X. Rozanska, D. Klahr, T. Guignon, and P. F. Lessard. Accelerating VASP electronic structure calculations using graphic processing units. *J. Comput. Chem.* 33, 2581 (2012). <https://doi.org/10.1002/jcc.23096>
44. M. Hutchinson and M. Widom, VASP on a GPU: Application to exact-exchange calculations of the stability of elemental boron. *Comput. Phys. Commun.* 7, 1422 (2011). <https://doi.org/10.1016/j.cpc.2012.02.017>
45. K. Momma and F. Izumi, VESTA 3 for three - dimensional visualization of crystal, volumetric and morphology data. *J. Appl. Crystallogr.* 44, 1272 (2011). <https://doi.org/10.1107/S0021889811038970>
46. Y. Watanabe, Ferroelectricity of stress-free and strained pure SrTiO₃ revealed by *ab initio* calculations with hybrid and density functionals, *Phys. Rev. B* 99, 064107 (2019). <https://doi.org/10.1103/PhysRevB.99.064107>
47. H. A. Hadi and R. A. Ismail, Energy band diagram of FTO/porous silicon Heterostructure, *J. Phys. Conf. Ser.* 1795 012016 (2021). [doi:10.1088/1742-6596/1795/1/012016](https://doi.org/10.1088/1742-6596/1795/1/012016)
48. S. Hasegawa, X. Tong, S. Takeda, N. Satoa, and T. Nagao, Structures and electronic transport on silicon surfaces, *Progress in Surf. Sci.* 60, 89 (1999). [https://doi.org/10.1016/S0079-6816\(99\)00008-8](https://doi.org/10.1016/S0079-6816(99)00008-8)
49. P. A. Anderson, Work function of gold, *Phys. Rev.* 115, 553 (1959).
50. D. E. Eastman, Photoelectric work functions of transition, rare-earth, and noble metals, *Phys. Rev. B* 2, 1 (1970). <https://doi.org/10.1103/PhysRevB.2.1>
51. A. Krozer and M. Rodahl, X-ray photoemission spectroscopy study of UV/ozone oxidation of Au under ultrahigh vacuum conditions, *J. Vac. Sci. Technol. A* 15, 1704 (1997). <https://doi.org/10.1116/1.580924>
52. H. Tsai, E. Hu, K. Perng, M. Chen, J.-C. Wu, and Y.-S. Chang, Instability of gold oxide Au₂O₃, *Surf. Sci.* 537, L447 (2003). [https://doi.org/10.1016/S0039-6028\(03\)00640-X](https://doi.org/10.1016/S0039-6028(03)00640-X)
53. L. K. Ono and B. R. Cuenya, Formation and thermal stability of Au₂O₃ on gold nanoparticles: size and support effects, *J. Phys. Chem., C* 112, 4676 (2008). <https://doi.org/10.1021/jp711277u>

54. S. Mader, R. Feder and P. Chaudhari, Recrystallization of (001) oriented gold films into (111) orientation, *Thin Solid Films* 14, 63 (1972). [https://doi.org/10.1016/0040-6090\(72\)90370-7](https://doi.org/10.1016/0040-6090(72)90370-7)
55. S.-H. Yoo, N. Siemer, M. Todorova, D. Marx, and J. Neugebauer, Deciphering charge transfer and electronic polarization effects at gold nanocatalysts on reduced titania support, *J. Phys. Chem. C* 123, 5495 (2019). <https://doi.org/10.1021/acs.jpcc.8b12015>